

Computational Study of Tip-Leakage Flow Around a Static Hydrofoil

Y. Jin^{1*}, D.A. Pook², J. A. Venning¹, P.S. Russell¹
L. Barbaca¹, B. W. Pearce¹, and P. A. Brandner¹

¹ Australian Maritime College, University of Tasmania, Tasmania, 7248, Australia

² Defence Science & Technology Group, Victoria, 3207, Australia

*Email: yuting.jin@utas.edu.au

Abstract

The flow field in the tip gap region between a rotating blade and a static casing is commonly referred to as tip-leakage flow (TLF). This flow is observed in many fluid mechanics applications such as axial turbomachinery and ducted propulsors. TLF features complex vortical structures with a high susceptibility to cavitation inception in water. The present work adopts the Reynolds-Averaged Navier-Stokes (RANS) equations, solved using ANSYS Fluent, to simulate the TLF of a static hydrofoil at a Reynolds number of 3×10^6 . This configuration was recently studied experimentally at the Australian Maritime College Cavitation Research Laboratory for tip gap spacing between 3.36 ~ 53.8 mm (0.1 to 1.6 times the maximum hydrofoil thickness). The objective of this study was to resolve the different vortices that exist within the TLF and accurately predict their minimum pressures, which is an important parameter for cavitation inception prediction. Computational fluid dynamics (CFD) simulations matched the experimental conditions, with the hydrofoil chord at an incidence angle of 6 degrees to the freestream flow and the same ceiling (casing) boundary layer thickness as in the experiment. Single-phase computations were carried out to assess the performance of different numerical configurations e.g. eddy viscosity and Reynolds stress turbulence models, wall resolved and wall functions, and grid resolution. Despite cell counts approaching 500 million, grid convergence of the simulations was not achieved with the predicted minimum vortex pressure still decreasing with grid refinement. However, comparison of the predicted tip-leakage vortex trajectory, and the predicted region where the static pressure fell below the vapour pressure, showed good agreement with observed cavitation regions from the experiments.

1. Introduction

Tip-leakage flow (TLF) is defined by the complex flow structures in the tip gap region of ducted propulsors and turbomachinery. This unsteady and highly turbulent flow often brings adverse effects such as blade efficiency loss, cavitation inception, and noise emission, which are yet to be understood completely. The fundamental nature of the TLF was experimentally studied by Inoue and Kuroumaru (1989), who revealed the leakage flow between the blade tip and the casing originated from the pressure difference between the blade pressure and suction sides. The roll-up of the vorticity generated by the leakage flow induced the formation of a tip-leakage vortex (TLV). Secondary scraping/induced vortices were found on the pressure side, near the trailing edge for small tip clearance, where the leakage flow rate was low. Measurements by Storer and Cumpsty (1990) showed the primary TLV increased in size and strength with increasing tip clearance and also shifted the location of minimum pressure in the vortex core downstream. In the last decade, a complex and problematic feature of the TLF was uncovered in the experiments of Devenport et al., (1999). The primary TLV was found to stretch small-scale secondary vortical filaments (SVF) formed at the blade tip, leading to instantaneous, lower pressure drops in the SVF when compared to the TLV core.

Alongside the development of experimental techniques, improvements in computational fluid dynamics (CFD) modelling were made to study TLF physics, mostly based on Reynolds-Averaged



Navier Stokes (RANS) and Large-Eddy Simulations (LES). You et al., (2007) analysed the trajectory and breakdown of the TLV using LES, finding the tip-leakage jet and TLV to produce strong mean velocity gradients, leading to the production of turbulent kinetic energy. They showed this mechanism to be mostly unchanged with tip-gap spacing. Boudet et al., (2016) adopted a zonal RANS/LES method for the fan tip-clearance flow and captured wandering of the TLV. Pogorelove et al., (2015) found at off-design operating conditions that the tip clearance vortex interacted with the downstream blade and generated a cyclic transition and peak pressure fluctuations on the suction side of the blade near the tip. They conducted a spectral analysis of the instantaneous velocity and pressure fields downstream of the blade and correlated the wandering motion of the TLV with low-frequency acoustic peaks. Decaix et al., (2015) compared LES and RANS approaches for computing TLF around the tip of a NACA foil. Both RANS and LES captured the primary vortex core location accurately compared to experimental data. Moghadam et al., (2019) performed detailed and comprehensive analyses of the tip vortex system of a ducted axial fan using LES. The results showed that increasing the tip-gap spacing resulted in several vortices in the tip-gap region, i.e., tip leakage, separation and induced vortices. Large tip-gap spacing enlarged the diameter and the strength of the primary tip vortex and decreased the efficiency of the ducted propulsor.

To form an initial assessment of CFD techniques to predict TLF, the flow field around a static NACA hydrofoil was computed using the RANS equations and compared with measurements from the Australian Maritime College (AMC) Cavitation Research Laboratory (CRL). Separate simulations solving the RANS equations with different near-wall grid resolutions (wall resolved vs wall functions) and turbulence closure models were conducted to assess their impacts on the predicted flow field. In addition, progressive grid refinements were carried out to resolve the pressure drop in the TLV core to a magnitude comparable to the experimental measurement.

2. CFD methods

3.1 Geometry and Flow Conditions

The hydrofoil used is a bespoke design from Russell et al., (2022) aimed at limiting face cavitation. The model had a chord (c) of 280 mm, and the span (s) could be varied between 540 mm and 610 mm, depending on the targeted tip gap clearance. The profile was based on a cambered NACA 66-012 section at the tip (top 30% of the span), with a max thickness (t) of 33.6 mm. The model was experimentally tested at a Reynolds number of 3.0×10^6 based on the chord length. The hydrofoil's leading edge was located approximately 900 mm downstream of the test-section entrance. The unperturbed wall boundary layer 99% thickness at the hydrofoil leading edge was 19 mm. The hydrofoil was set at an angle of incidence of 6 degrees.

3.1 CFD Domain Setup

The computational domain resembles the test section of the AMC CRL, as shown in Figure 1(a). To match the wall boundary layer thickness with the experiment, the CRL contraction was simulated to produce an inlet velocity field for the test section. This was then used as an inlet boundary condition for simulations with only the test section, a truncated downstream diffuser with uniform cross-section, and the hydrofoil. The top, bottom and sides of the domain were set as the non-slip wall boundaries. The downstream boundary condition was a pressure outlet boundary.

3.1 Solver and Grid

The RANS equations were solved using ANSYS Fluent's incompressible, pressure-based solver with SIMPLEC pressure-velocity coupling. Only single-phase flow was simulated (no cavitation). The turbulence closure terms of the RANS equations were modelled with the $k-\omega$ SST turbulence model with curvature correction (default correction factor of 1), and the Baseline Reynolds stress model (BSL-RSM). Gradients were calculated with the Green-Gauss cell-based method. The

turbulent kinetic energy and specific dissipation rate in the $k-\omega$ SST turbulence model and the Reynolds stress terms in the BSL-RSM turbulence model were discretised with a second-order upwind scheme, while the momentum term was solved using the third-order MUSCL scheme. Although not shown in this paper, applying MUSCL scheme on solving the momentum term was found to reduce (improve) the calculated pressure in the TLV on a given grid. Both wall-resolved, $y^+ = 1$, and wall-modelled $30 < y^+ < 100$ grids were studied to understand the influence on resolving the pressure field within the TLF. Two base grid types were created, a poly-hexcore grid using a hybrid mix of hexahedron and polyhedron elements, and a multi-block structured grid as shown in Figure 1(d-e). Local surface refinements were employed to the hydrofoil tip and trailing edge surfaces for better resolving geometrical details. Volumetric refinements were applied to the region where the tip-leakage and trailing edge vortices existed. For the structured grid, adaptive mesh refinements were applied to the TLV core to more accurately resolve the local pressure drops. A summary of cell counts for the presented computational cases is provided in Table 1 with an approximate number of cells located within the TLV core. Several cut planes in the x -axis along the computational domain were created to examine velocity and pressure fields.

Grid	Poly-hexcore		Structured grid	
	Total ($\times 10^6$)	within TLV core ($\times 10^6$)	Total ($\times 10^6$)	within TLV core ($\times 10^6$)
Base grid (ref-0)	106.0	0.5	132.0	0.2
First refinement (ref-1)	134.8	3.9	133.6	1.8
Second refinement (ref-2)	341.6	31.4	146.4	14.6
Third refinement (ref-3)	n.a	n.a	247.6	115.7

Table 1. Cell counts for the CFD grids, volumetric mesh refinement on the poly-hexcore grid and adaptive mesh refinement on the structured grid.

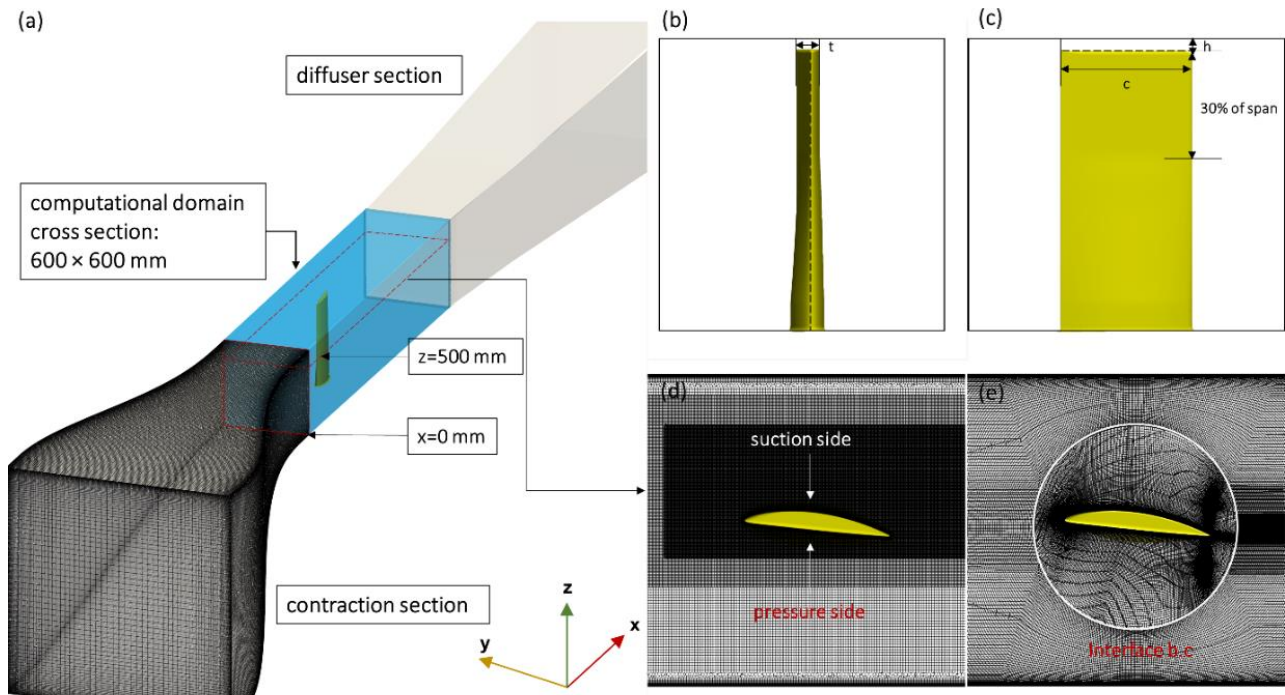


Figure 1. (a) Schematic view of the computational domain; (b-c) hydrofoil geometry; (d) poly-hexcore grid ref-0, 224 cells along chord, 666 cells along span; (e) structured grid ref-0, 254 cells along chord, 401 cells along span

3. Results

3.1 Tip-leakage Flow Characteristics

Three different vortices were identified in the tip-gap region: the tip-leakage vortex, the tip-separation vortices, and the induced vortex. The vortical structures are presented in Figure 2 by the iso-surface of the non-dimensional second-invariant of the velocity gradient tensor (Haller, 2005),

$$Q^* = \frac{1}{2}(|\boldsymbol{\Omega}|^2 - |\boldsymbol{S}|^2) \times (c^2/U_\infty^2), \quad (1)$$

$$\boldsymbol{\Omega} = \frac{1}{2}(\nabla\boldsymbol{v} - \nabla\boldsymbol{v}^T), \quad (2)$$

$$\boldsymbol{S} = \frac{1}{2}(\nabla\boldsymbol{v} + \nabla\boldsymbol{v}^T), \quad (3)$$

where $\boldsymbol{\Omega}$ is the vorticity tensor, \boldsymbol{S} is the rate-of-strain tensor, $\nabla\boldsymbol{v}$ is the velocity gradient tensor and U_∞ is the free stream velocity magnitude. A non-dimensional value of 50 is used for the iso-surface. The tip gap spacing, τ , non-dimensionalised by the airfoil maximum thickness t , was 0.4. Here, the TLV was the primary flow feature captured, which was generated by the roll-up of the tip-leakage jet. The induced vortices, also referred to as scraping vortices in some literature, were found next to the TLV, rotating in the opposite direction. A series of small tip-separation vortices were formed due to flow separation and shed from the suction side of the blade tip surface. These secondary vortices spiral around/merge with the main TLV as the flow developed. Also shown on the Q^* iso-surface are contours of the pressure coefficient, C_p , defined as $(p - p_\infty)/(0.5\rho U_\infty^2)$, where p is the static pressure, p_∞ is the free stream reference pressure and ρ is the water density. A low-pressure region was observed in the core of the TLV, consistent with literature when considering the mean pressure.

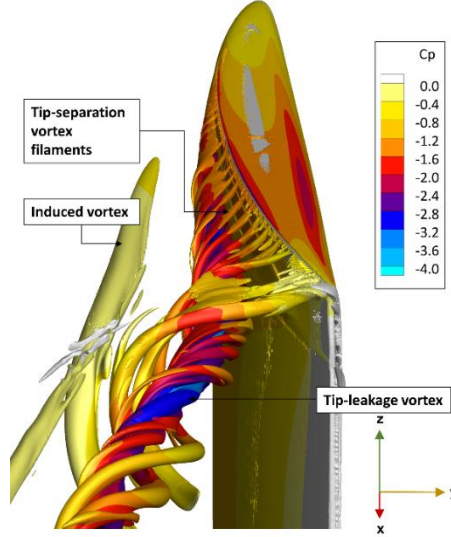


Figure 2. Reynolds-averaged vortical structures for $\tau=0.4$ represented by dimensionless $Q^*=50$, computed using poly-hexcore grid ref-2 with BSL-RSM turbulence model

Figure 3 shows images of cavitation bubble development (white colour) for varying tip gap spacings from the experiment of (Russell et al., 2022) at the cavitation number (σ) of 1.35. The cavitation number, σ , is defined as $(p_\infty - p_v)/(0.5\rho U_\infty^2)$, where p_v is the water vapour pressure. The x and y -axis here are longitudinal and lateral coordinates, where $x/c = 0$ corresponds to a position 200 mm downstream of the entrance to the test section and $y/c = 0$ refers to the mid-point across its width. Overlaid are the iso-surfaces (blue colour) at $C_p = -1.35$ from the single-phase CFD simulations, where the static pressure just fell below the vapour pressure. The iso-surfaces agreed well with the extent of cavitation observed in the experiment. The TLV trajectory changed

significantly with tip gap spacing, moving away from the hydrofoil with decreasing τ . In the experiments of Russell et al., (2022), cavitation inception was found on the pressure side of the tip due to the low-pressure region formed. Again, the iso-surface at $C_p = -1.35$ from the present simulations shows reasonable agreement with this location of cavitation onset. The pressure-side low-pressure region extended upstream as τ decreased. According to Boulon et al., (1999) and Russell et al., (2020), this is an inviscid phenomenon related to the proximity of the wall, whereby reducing tip gap distance leads to a larger incidence flow angle around the tip of the hydrofoil. However, for the smallest tip gap spacing $\tau=0.1$, the pressure-side cavitation was not apparent.

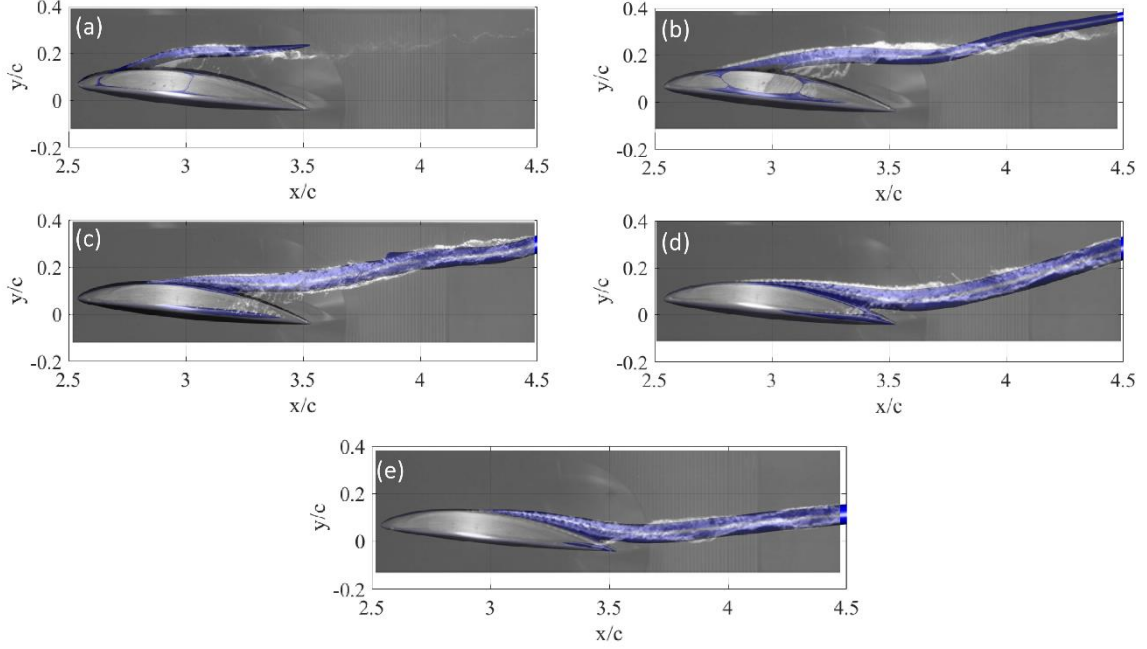


Figure 3. CFD predicted iso-surface at $C_p=-1.35$ (blue colour) compared with experimentally measured cavitation topology (white colour) for varying tip gap spacing: (a) $\tau=0.1$, (b) $\tau=0.2$, (c) $\tau=0.4$, (d) $\tau=0.8$ and (e) $\tau=1.6$ at $\alpha=6^\circ$, $Re=3 \times 10^6$, $\sigma=1.35$

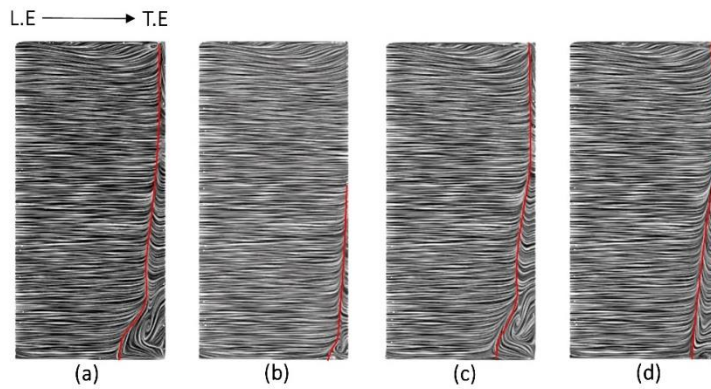


Figure 4. Line integral convolution of the wall-shear stress on the suction side of the hydrofoil for the case, $\tau=0.4$, $\alpha=6^\circ$, $Re=3 \times 10^6$: (a) $k-\omega$ SST CC $y^+ = 30$, Lift = 7913 N. (b) BSL-RSM $y^+ = 30$, Lift = 8964 N. (c) $k-\omega$ SST CC $y^+ = 1$, Lift = 7819 N. (d) BSL-RSM $y^+ = 1$, Lift = 8030 N.

3.2 Hydrofoil Loads and Surface Wall-shear Stress

The TLF is dependent on not only the tip gap spacing and incoming ceiling boundary layer but the lift of the hydrofoil which is dependent on boundary layer attachment/separation. Establishing the validity of wall-functions for this flow is important for future studies that might employ wall-modelled approaches. Figure 4 shows the wall-shear stress on the hydrofoil surface from CFD

simulations with different turbulence models and y^+ . The topology in the near tip region (top side of the figure) is similar for all cases. However, separation just upstream of the trailing edge at the root of the foil is present. This separation will affect the total lift which was not measured in the experiment. The trailing edge separation and lift differ with y^+ for the BSL-RSM model, while results from the $k-\omega$ SST model are more consistent. However, without experimental loads and surface flow visualization, a conclusive assessment of the appropriateness of wall-modelling can not be made.

3.3 Pressure within Tip-leakage Vortex Core

At a high Reynolds number, although cavitation inception may originate from vortical filaments formed by stretching of the trailing edge and tip separation vortices, the mean pressure minimum generally exists in the core of the TLV. Figure 5 gives an example of the Reynolds-averaged pressure coefficient at different streamwise slices along the TLV and tracks the C_p min location. Here, the initiation of TLV was found between 70 ~ 80 mm (25 ~ 28.6 % of chord length) from the leading edge of the foil. Figure 5 also shows the movement of the TLV detachment from the tip to the pressure side is sensitive to wall-modeling.

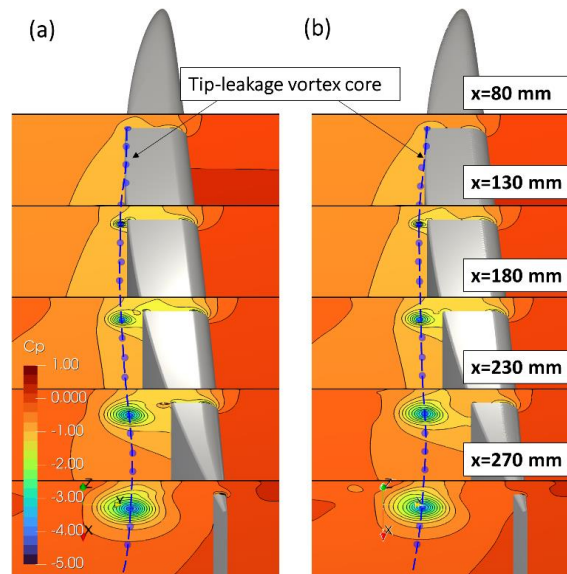


Figure 5. Contours of C_p distribution along the TLV core for the case, $\tau=0.4$, $\alpha=6^\circ$, $Re=3 \times 10^6$, BSL-RSM, poly-hexcore grids (a) $y^+ = 1$ and (b) $y^+ = 30$, where x is relative to the leading edge

In addition to wall y^+ and turbulence models, the impact of grid resolution on the pressure drop in the TLV core was studied for the gap clearance of $\tau=0.4$. The minimum pressure coefficients at each streamwise position along the TLV from both the poly-hexcore and structured grids are presented in Figure 6. Even with the multiple stages of grid refinement localised to the TLV core, grid independence was not achieved. Compute resources have limited further grid refinement.

C_p along the TLV core predicted by the poly-hexcore and structured grids showed a consistent trend after refinements were applied. Abnormal pressure bumps were observed in the coarse poly-hexcore grid solutions (ref-0 and ref-1) at around $x/c=3.0$ (140 mm from the leading edge) when the TLV passed through the layer of grid that bridged the polyhedron prism layers and outer domain hexahedron cells. This issue disappeared when volumetric refinements were applied, introducing more polyhedron cells into this transitional region. The magnitude of the global C_p minimum was found to be sensitive to grid resolutions in the TLV vortex core, even though the iso-surface at $C_p = -1.35$ shown in Figure 6(a) remained unchanged through grid refinement. According to measurements by Russel et al., (2022), the magnitude of the global C_p minimum for this case was approximately -6.50. After refining the TLF region, the CFD prediction approached this value

gradually, with the global C_p minimum values monotonically converging with increased grid refinement. However, under 500 million cell count (poly-hexcore ref-2 = 341 million; structured grid ref-3 = 248 million), grid converged global C_p minimum was still not achieved in either the poly-hexcore or the structured grid solution.

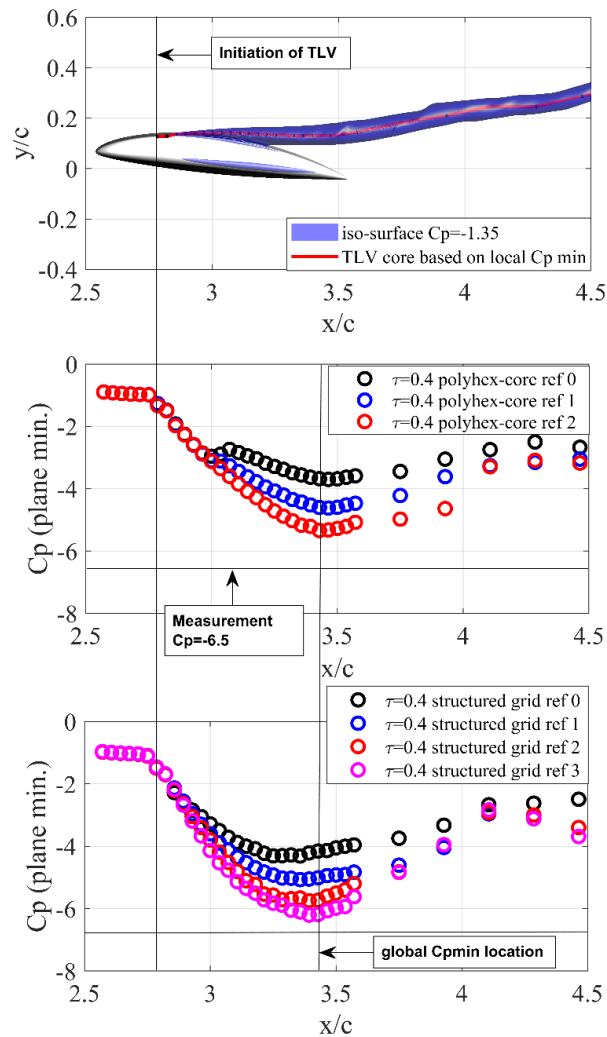


Figure 6. Pressure drops in the TLV core for test case, $\tau=0.4$, $\alpha=6^\circ$, $Re=3 \times 10^6$ computed with y^+ of 1 grids using BSL-RSM turbulence model: (a) line representation of TLV core, (b) C_p predictions from poly-hexcore grids and (c) C_p predictions from structured grids

4. Conclusions

Following the recent experiments carried out at AMC CRL, the TLF of a static hydrofoil has been computed using RANS-based CFD assuming all boundary layers were turbulent. A trailing edge flow separation was predicted on the hydrofoil, which alters the lift, and possibly the TLF of interest. Further investigation is required to determine if wall-functions can accurately model this flow, which has implications for the application of Detached Eddy Simulation or wall-modeled LES methods for this flow.

Different types of vortices in a typical TLF were observed from the RANS results, which were categorised as tip-leakage, tip-separation and induced vortices. The Reynolds-averaged pressure field indicated a global pressure minimum within the core of the TLV. When reducing gap clearance, the TLV was found to deflect away from the hydrofoil as a result of increased effective flow incident

angle. The iso-surfaces of $C_p = -1.35$ from RANS computations showed good agreement with the TLV's primary cavitation topology in the experiment at $\sigma = 1.35$.

The magnitude of the global C_p minimum was not grid-converged in the simulations presented, but a monotonic trend approaching the expected value was apparent. To achieve grid-independent pressure drops within the TLV core, total cell counts approaching, and likely in excess of, 500 million cells are required with the finite volume differencing schemes and grids used. On the other hand, grid convergence on drag and lift forces was achieved with a significantly lower cell count.

References

- Boudet, J., Caro, J., Li, B., Jondeau, E., & Jacob, M. C. (2016). Zonal large-eddy simulation of a tip leakage flow. *International Journal of Aeroacoustics*, 15(6–7), 646–661. <https://doi.org/10.1177/1475472X16659215>
- Boulon, O., Callenaere, M., Franc, J. P., & Michel, J. M. (1999). An experimental insight into the effect of confinement on tip vortex cavitation of an elliptical hydrofoil. *Journal of Fluid Mechanics*, 390, 1–23. <https://doi.org/10.1017/S002211209900525X>
- Decaix, J., Balarac, G., Dreyer, M., Farhat, M., & Münch, C. (2015). RANS and les computations of the tip-leakage vortex for different gap widths. *Journal of Turbulence*, 16(4), 309–341. <https://doi.org/10.1080/14685248.2014.984068>
- Devenport, W. J., Vogel, C. M., & Zsoldos, J. S. (1999). Flow structure produced by the interaction and merger of a pair of co-rotating wing-tip vortices. *Journal of Fluid Mechanics*, 394, 357–377. <https://doi.org/10.1017/S0022112099005777>
- Haller, G. (2005). An objective definition of a vortex. *Journal of Fluid Mechanics*, 525, 1–26. <https://doi.org/10.1017/S0022112004002526>
- Inoue, M., & Kuroamaru, M. (1989). Structure of Tip Clearance Flow in an Isolated Axial Compressor Rotor. *Journal of Turbomachinery*, 111(3), 250–256. <https://doi.org/10.1115/1.3262263>
- Moghadam, S. M. A., Meinke, M., & Schröder, W. (2019). Analysis of tip-leakage flow in an axial fan at varying tip-gap sizes and operating conditions. *Computers and Fluids*, 183, 107–129. <https://doi.org/10.1016/j.compfluid.2019.01.014>
- Pogorelov, A., Meinke, M., & Schröder, W. (2015). Cut-cell method based large-eddy simulation of tip-leakage flow. *Physics of Fluids*, 27(7). <https://doi.org/10.1063/1.4926515>
- Russell, P. S., Barbaca, L., Russell, E. S. C., Pearce, B. W., & Brandner, P. A. (2020). Cavitation in Tip-Leakage Flows. *33rd Symposium on Naval Hydrodynamics, June*.
- Russell, P. S., Barbaca, L., Venning, J. A., Pearce, B. W., & Brandner, P. A. (2022). The influence of nucleation on cavitation inception in tip-leakage flows. *34th Symposium on Naval Hydrodynamics, July*.
- Storer, J. A., & Cumpsty, N. A. (1990). Tip leakage flow in axial compressors. *Proceedings of the ASME Turbo Expo, 1*. <https://doi.org/10.1115/90-GT-127>
- You, D., Wang, M., Moin, P., & Mittal, R. (2007). Vortex dynamics and low-pressure fluctuations in the tip-clearance flow. *Journal of Fluids Engineering, Transactions of the ASME*, 129(8), 1002–1014. <https://doi.org/10.1115/1.2746911>